Materials Advances

ROYAL SOCIETY OF CHEMISTRY

PAPER

View Article Online
View Journal | View Issue

Cite this: *Mater. Adv.*, 2026, 7, 4360

An integrated DFT–FDTD design of plasmon-enhanced lead-free $CsSn_xGe_{1-x}I_3$ perovskite LEDs

Shoumik Debnath,[a] Sudipta Saha,[a] Khondokar Zahin,[a] Ying Yin Tsui[b] and Md Zahurul Islam *[a]

$CsSn_xGe_{1-x}I_3$ as lead-free perovskites are promising for next generation NIR emitting perovskite light emitting diodes (PeLEDs) due to their tunable bandgaps and stability. However, they suffer from poor light extraction efficiency (LEE), and accurate composition-specific optical data for these materials remain scarce. This study presents a density functional theory (DFT) informed finite-difference time-domain (FDTD) framework to optimize light extraction *via* compositional tuning and plasmonic enhancement. First, DFT calculations were performed to obtain composition-specific complex refractive index and extinction coefficient values for x = 0, 0.25, 0.5, 0.75, and 1. Results showed that the bandgap increased from 1.331 eV for $CsSnI_3$ to 1.927 eV for $CsGeI_3$ with increasing Ge content, while the refractive index ranged from 2.2 to 2.6 across compositions. These optical constants were then used as inputs for FDTD simulations of a PeLED structure with optimized Au/SiO_2 core–shell nanorods for plasmonic enhancement. A 12.1-fold Purcell enhancement was achieved for $CsSn_{0.25}Ge_{0.75}I_3$, while LEE reached 25% for $CsSn_{0.5}Ge_{0.5}I_3$. A LEE enhancement of 36% was obtained for $CsSnI_3$, and spectral overlap between emitter and plasmon resonance reached 96% for Sn-rich compositions. Among the studied compositions, $CsSn_{0.5}Ge_{0.5}I_3$ provides the best balance between emission enhancement, light extraction efficiency (25%), Purcell enhancement (5.3×), spectral matching (93%), and oxidation stability, while Ge-rich alloys exhibit stronger spontaneous emission rate enhancement. These results establish composition-aware design guidelines for lead-free perovskite emitters targeting flexible and wearable optoelectronic applications.

Received 23rd January 2026,
Accepted 21st March 2026

DOI: 10.1039/d6ma00110f

rsc.li/materials-advances

1. Introduction

PeLEDs have rapidly emerged as promising candidates for next-generation light sources, including applications in displays,[1–3] wearable electronics, and flexible optoelectronics.[4,5] This rapid advancement has been made possible because of the exceptional optoelectronic properties of metal halide perovskites (MHPs), including high absorption coefficients, solution processability, and tunable emission characteristics.[6] The external quantum efficiency (EQE) of these devices has surged from less than 1% in early demonstrations[7] to over 28% for red,[8] 30% for green,[9] and 23% for blue emitters.[10] This positions PeLEDs as serious competitors to already established organic LED (OLED) technology.[1]

Apart from these efficiency gains, PeLEDs offer several other distinct advantages that make them attractive for commercial applications. These advantages, combined with narrow emission linewidths (FWHM typically <20 nm), bandgap tunability across visible to NIR wavelengths, and low-cost solution processing,[11–16] position PeLEDs as strong candidates for next-generation displays and flexible optoelectronics.

Although EQE has reached up to 32%,[17] the inherent toxicity of Pb is a major barrier to commercialization of these optoelectronic devices.[9,18–20] Thus, developing lead-free alternatives is a research priority to ensure environmental safety and sustainability.[4,14,21] Also, for commercial applications, operational lifetimes should exceed 10 000 hours and manufacturing costs should remain below USD 100 m^{-2}.[22] These targets are still unachieved for both lead-based and lead-free systems. This leaves significant room for innovation in both materials engineering and device architecture optimization.

The search for Pb substitutes has focused on tin (Sn^{2+}) and germanium (Ge^{2+}), which share comparable ionic radii and valence states with Pb^{2+}.[18,21] Sn-based PeLEDs have

[a] *Department of Electrical and Electronic Engineering, Bangladesh University of Engineering and Technology, Dhaka 1000, Bangladesh. E-mail: mdzahurulislam@eee.buet.ac.bd*
[b] *Department of Electrical and Computer Engineering, University of Alberta, Edmonton, AB T6G 2H5, Canada*

demonstrated external quantum efficiencies (EQEs) of up to 20.29% with a narrow emission bandwidth of 24.9 nm,[12] while Ge–Pb mixed PeLEDs have exhibited photoluminescence quantum yields (PLQYs) of nearly 71% and EQEs around 13%.[23] Sn-based MHPs exhibit excellent optoelectronic properties with direct bandgaps ranging from 1.2 eV to 1.4 eV, emitting in the near-infrared (NIR) region.[18] Recent experimental demonstrations have achieved $CsSnI_3$-based NIR PeLEDs with external quantum efficiencies of up to 7.6% and emission wavelengths of 930–950 nm.[24–26]

However, both Sn- and Ge-based MHPs suffer from oxidation-induced instability, where Sn^{2+} and Ge^{2+} ions readily oxidize to Sn^{4+} and Ge^{4+}, forming deep defects that degrade long-term performance.[12,18] This intrinsic chemical instability of Sn^{2+} arises from its relatively low Sn^{2+}/Sn^{4+} redox potential, causing spontaneous oxidation in both precursor solutions and deposited thin films.[27]

Partial substitution of Sn^{2+} with Ge^{2+} has proven particularly effective in mitigating this instability.[28,29] Ge alloying forms a native GeO_x layer on the perovskite surface, which acts as a protective barrier against environmental factors such as moisture and oxygen.[30] $CsSn_{0.5}Ge_{0.5}I_3$-based devices have demonstrated stable operation with less than 10% efficiency degradation over 500 hours of continuous operation,[30] representing a significant advancement in operational stability for lead-free systems. This concept, first demonstrated in perovskite photovoltaics, has led to simultaneous improvements in both power conversion efficiency and long-term stability.[18] Compositionally tuned $CsSn_xGe_{1-x}I_3$ systems therefore represent a promising alternative to lead-based perovskites for next-generation optoelectronic devices.

However, the high refractive index ($\sim$2.5) of these perovskites limits the outcoupling efficiency to approximately 8%.[1,31] This poor outcoupling happens because the perovskite's high refractive index traps most of the light. Studies show that nearly 80% of the generated photons never escape the device.[32] The primary reason behind it is total internal reflection at material interfaces. This alone accounts for nearly 56% of total radiative power loss.[31,33] Thus, enhancing LEE is a critical step towards realizing highly efficient lead-free PeLEDs.

To model light extraction properly, we need accurate wavelength-dependent n and k values for the perovskite emitter.[34,35] Existing optical simulations often reuse generic or oversimplified n, k datasets resulting in substantial inaccuracies. Generic optical constants and purely geometric models cause inaccuracies in capturing the complex wave-optical behavior of light.[36] Such inaccuracies lead to spectral mismatch between the emitter's photoluminescence and the device's cavity modes. As a result, LEE predictions become unreliable and far-field radiation pattern characteristics become distorted.[34]

First-principles DFT calculations are a robust approach to counter this problem. DFT calculations determine optimized geometrical structures[5] along with accurate electronic structures and optical properties.[37] This methodology has been widely used to investigate the optical and intrinsic electronic properties of MHPs,[5,9,38] including Sn-based MHPs ($CsSnX_3$).[2] This approach eliminates reliance on extrapolated or approximate n, k values.

However, DFT cannot model the electromagnetic interactions that govern light propagation and extraction within PeLEDs.[31] Therefore, to address this issue, DFT-driven electromagnetic modeling is required. The FDTD method is a powerful approach that numerically solves Maxwell's equations in the time domain.[39] This enables quantitative analysis of field distributions, resonant cavity effects, and photon outcoupling pathways.[1] Using DFT-derived n and k values as inputs, FDTD simulations can be used to calculate key performance metrics of PeLEDs. These include the Purcell factor, LEE, radiated power, spectral overlap, and far-field emission profiles.[31,39]

Plasmonic coupling by embedding metallic nanoparticles is an effective strategy to improve light extraction in PeLEDs.[32] This helps to overcome intrinsic optical limitations. Noble metal nanoparticles localize electromagnetic energy *via* surface plasmon resonance to enhance emission in PeLEDs.[40] Among different nanoparticle geometries, Au nanorods (NRs) offer superior chemical stability and oxidation resistance compared to Ag, along with enhanced local density of optical states (LDOS) that improves radiative recombination.[41] The longitudinal plasmon resonance of Au NRs can be tuned *via* aspect ratio control to align with NIR emission wavelengths,[42] making them particularly suitable for enhancing NIR-emitting $CsSn_xGe_{1-x}I_3$ through optimized spectral overlap and Purcell enhancement. Since Au is biocompatible and resistant to environmental degradation, it is well suited for wearable and flexible optoelectronic applications.[43]

Despite recent progress in lead-free perovskites, the relationship between Ge substitution and the optical properties of $CsSn_xGe_{1-x}I_3$ PeLEDs has not been systematically investigated. Previous studies have focused primarily on stability improvements and bandgap tuning for photovoltaics, leaving the impact of Ge alloying on LED emission profiles, plasmonic interactions, and far-field characteristics largely unexplored.

We address this gap through an integrated DFT–FDTD framework that, for the first time, establishes quantitative links between Ge substitution, composition-specific optical properties, and device-level light extraction performance in $CsSn_xGe_{1-x}I_3$ PeLEDs. We compute wavelength-dependent n and k values directly from DFT for each composition, enabling physically accurate electromagnetic modeling of emission enhancement, plasmonic coupling with Au NRs, and far-field radiation characteristics. We also optimize NR geometries across x = 0 to 1 to achieve high LEE, Purcell enhancement, and spectral overlap. This makes NIR emission in device architectures compatible with flexible, wearable applications.

This paper is organized into four sections. Section 2 discusses computational methods for material and device analysis. Results and discussion are presented in Section 3, and Section 4 concludes the work.

2. Computational methods for material and device analysis

Our computational approach connects atomic-scale physics with device-scale optics by combining DFT and FDTD simulations.

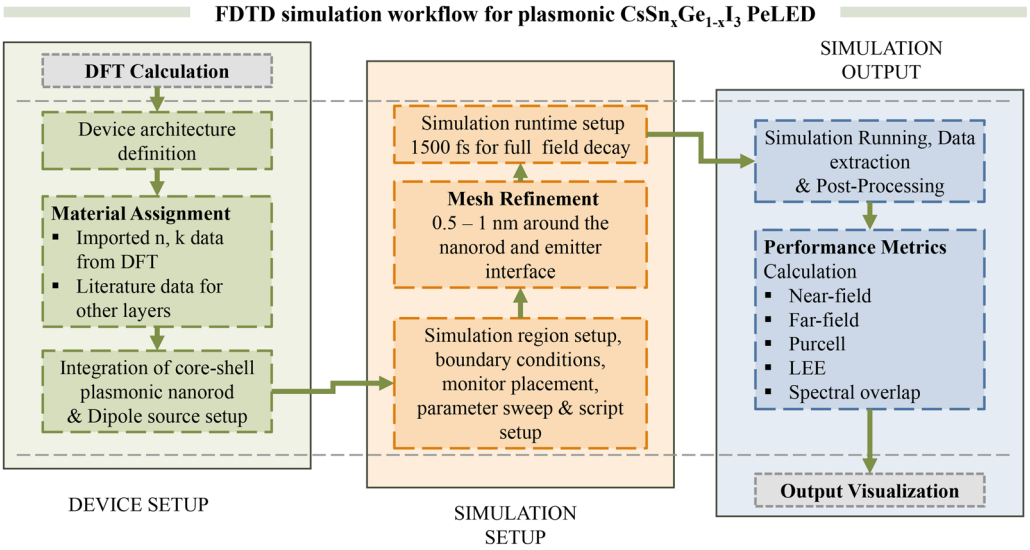

Fig. 1 Computational workflow for FDTD simulation of plasmonic $CsSn_xGe_{1-x}I_3$-based PeLEDs. The device setup incorporates DFT-derived optical constants for the perovskite layer alongside literature data for other materials. FDTD simulations employ refined meshing near critical interfaces and integrate Au/SiO_2 NRs at the ZnO/perovskite boundary. Performance analysis yields near-field and far-field distributions, Purcell factors, light extraction efficiency, and spectral overlap metrics, enabling composition-dependent device optimization.

DFT provides the composition-dependent refractive index (n) and extinction coefficient (k) of $CsSn_xGe_{1-x}I_3$ alloys, capturing their underlying electronic structure. These optical constants are then used as inputs for FDTD simulations of the complete PeLED architecture, enabling quantitative analysis of light emission, plasmonic enhancement, and spectral overlap with compositional accuracy.

2.1. First-principles calculations of material properties

DFT calculations were performed using the CASTEP module in Materials Studio 2020. The study utilized generalized gradient approximation (GGA) with the Perdew–Burke–Ernzerhof (PBE) exchange–correlation functional for geometry optimization. To mitigate bandgap underestimation by the PBE algorithm, we used the hybrid functional Heyd–Scuseria–Ernzerhof (HSE06) for band structure calculations. The properties were calculated by incorporating spin–orbit coupling (SOC). All calculations employed an ultrasoft pseudopotential with a plane-wave basis set and a cutoff energy of 500 eV. For the Brillouin zone sampling, a Monkhorst–Pack k-point grid of $6 \times 6 \times 6$ was used. The geometry of $CsSn_xGe_{1-x}I_3$ was relaxed until the energy and force reached the criteria of convergence at 1.0×10^{-6} eV and 0.01 eV $Å^{-1}$ between two adjacent steps.

2.2. Device level optical modeling of the perovskites

3D FDTD simulations were performed using Lumerical FDTD (Ansys Inc.) to investigate the optical response of plasmonic $CsSn_xGe_{1-x}I_3$-based PeLEDs. The FDTD algorithm solves Maxwell's equations numerically in the time domain, allowing modeling of light propagation, near-field enhancement, and resonant-cavity effects in multilayer optoelectronic structures.[44] The computational workflow for FDTD simulations is shown in Fig. 1.

The simulated PeLED adopted an architecture of ITO (100 nm)/Spiro-OMeTAD (35 nm)/$CsSn_xGe_{1-x}I_3$ (50 nm)/ZnO (40 nm)/Ag (100 nm), matching experimentally achievable stacks (Fig. 2a). Fig. 2b presents the energy-band diagram of the ITO/Spiro-OMeTAD/$CsSn_xGe_{1-x}I_3$/ZnO/Ag structure, showing hole injection from ITO into Spiro-OMeTAD, electron injection from Ag into ZnO, and carrier recombination within the perovskite layer. The present framework focuses exclusively on electromagnetic modeling of light emission and extraction. Electrical transport phenomena, including carrier injection barriers, mobility variations across compositions, and recombination zone distribution, are not explicitly simulated. Radiative recombination is assumed to occur uniformly within the emissive layer. Therefore, the model should be interpreted as an optical design study rather than a fully coupled electro-optical device simulation. Integration with drift-diffusion carrier transport modeling represents an important direction for future work.

Composition-dependent n, k spectra for the perovskite layer were derived from DFT calculations and imported into the FDTD material database. Optical constants for the remaining layers were taken from established datasets.[45–48] Spontaneous emission within the perovskite layer was represented by an electric dipole source positioned above the plasmonic nanostructure, radiating across the visible and NIR wavelengths corresponding to the emission window of $CsSn_xGe_{1-x}I_3$ compositions (Fig. 3). This source model treats electron–hole radiative recombination as an oscillating dipole and reproduces Purcell-enhanced emission in resonant photonic environments.[49] For plasmonic enhancements, a gold core–shell structured NR (Fig. 3) was positioned near the ZnO/perovskite interface, with SiO_2 acting as the shell to protect charge carriers from quenching.[50] If the emitter is placed too close to the

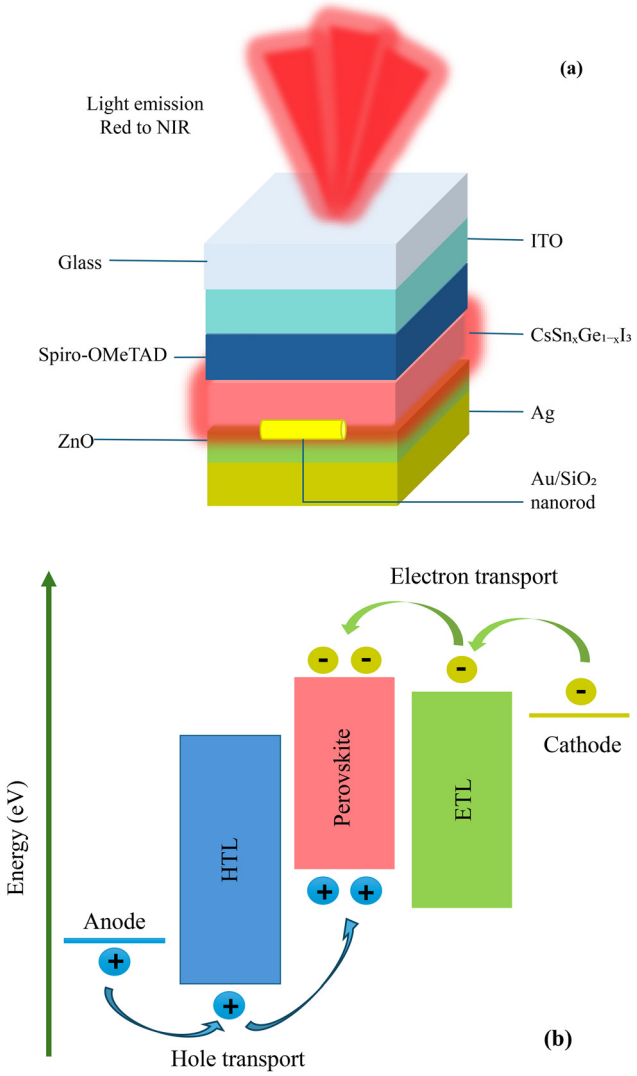

Fig. 2 (a) Layered device architecture of the $CsSn_xGe_{1-x}I_3$-based PeLED, illustrating the anode/HTL/perovskite/ETL/cathode stack and the upward light-emission direction. (b) Energy-band diagram of the ITO/Spiro-OMeTAD/$CsSn_xGe_{1-x}I_3$/ZnO/Ag structure, showing hole injection from ITO into Spiro-OMeTAD, electron injection from Ag into ZnO, and carrier recombination within the perovskite layer.

metal surface, non-radiative energy transfer to the metal dominates and net quenching occurs. The SiO_2 shell surrounding the Au nanorod was therefore fixed at a thickness of 5 nm. This separation distance was selected on the basis of established distance-dependent fluorescence measurements,[51] which show that the quenching regime dominates at separations below approximately 4 nm. By operating at 5 nm, the design places the emitter within the region of strong near-field enhancement while maintaining a margin above the quenching threshold. A full parametric sweep of shell thickness is identified as a clear direction for further work. The NR diameter and length were tuned so that the localized surface plasmon resonance (LSPR) spectrally overlapped with the composition-dependent emission peak. This produced strong near-field coupling and enhanced radiative decay.[52,53] The frequency-dependent dielectric function of gold was defined according to the Palik dataset.[46]

Periodic boundary conditions were applied in the lateral (x–y) directions to emulate an infinite emitter array, while perfectly matched layer (PML) boundaries were implemented vertically (z) to suppress spurious reflections.[54] This configuration reproduces realistic outcoupling behavior and has been validated for photonic-band-structure and plasmonic-resonator analyses.[55] A non-uniform spatial mesh was adopted, with refinement to 0.5–1 nm around the NR and emitter interface, gradually coarsening elsewhere to maintain computational efficiency. Each simulation was executed for 1500 fs, ensuring full electromagnetic-field decay before Fourier transform. From the computed field data, several key optical metrics were extracted.

In this study, LEE is calculated from the power collected by a far-field transmission monitor positioned above the ITO layer and normalized to the emitted dipole power within the simulation domain. This approach quantifies the fraction of radiative power that escapes the device stack into free space. While this method accurately captures total far-field radiation, a detailed modal decomposition of individual loss channels such as surface plasmon polariton (SPP) modes, waveguide modes, and metal absorption pathways was not explicitly performed. Such separation would require additional eigenmode analysis or volumetric absorption monitors for each layer. Furthermore, the dipole source used in the FDTD simulations represents an idealized radiative recombination event. Non-radiative recombination mechanisms such as trap-assisted recombination, Auger recombination, polaronic effects, and defect-induced quenching are not included in the present electromagnetic model. Therefore, the calculated Purcell factors describe the enhancement of the radiative decay channel only. Consequently, the reported LEE assumes unity internal quantum efficiency (IQE). In realistic devices, the EQE is related to the LEE through EQE = IQE × LEE, so the reported LEE values represent an optical upper limit. Practical efficiencies will depend heavily on material defect density and carrier recombination dynamics. While Au nanorods enhance the local density of optical states, they also introduce intrinsic ohmic absorption losses governed by the imaginary part of the metal dielectric function. Because the optical constants of Au in our FDTD model are taken from the Palik experimental dataset, all frequency-dependent absorption is accounted for in the electromagnetic energy budget. Power absorbed within the nanorod contributes to the difference between the total Purcell enhancement and the far-field LEE. The present FDTD framework does not include thermal modeling. The time-averaged volumetric heat source density in the Au nanorod, $Q = \frac{1}{2}\omega\varepsilon_0 \mathrm{Im}[\varepsilon_{\mathrm{Au}}]|\mathbf{E}|^2$, can be extracted from the computed field data and used as input to a heat diffusion solver in future work. For LED operation under spontaneous emission conditions at moderate power densities, the temperature rise from ohmic dissipation is expected to remain small. Nonetheless, a rigorous

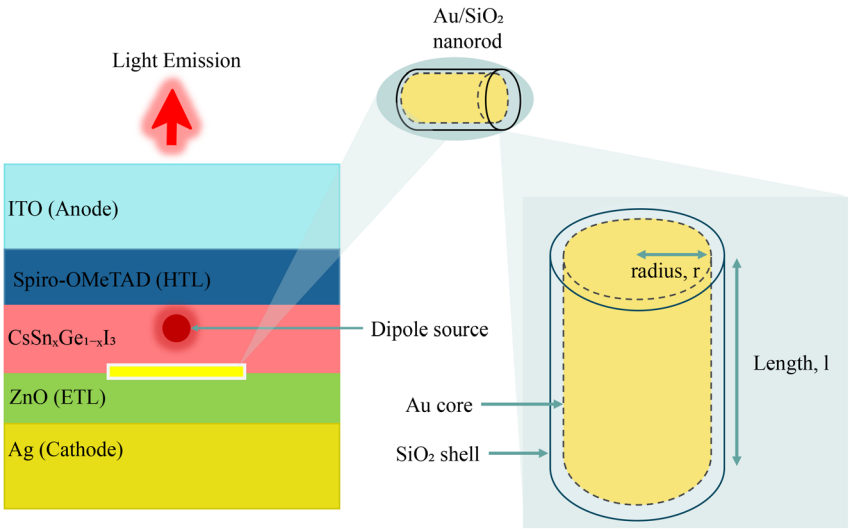

Fig. 3 Schematic illustration of the $CsSn_xGe_{1-x}I_3$-based PeLED structure incorporating a plasmonic Au/SiO_2 nanorod. The device stack (ITO/Spiro-OMeTAD/$CsSn_xGe_{1-x}I_3$/ZnO/Ag) includes a dipole emitter positioned near the embedded Au/SiO_2 core–shell nanorod to enable plasmon–emitter coupling. The nanorod geometry is defined by the Au core length (l) and radius (r), surrounded by a SiO_2 shell.

coupled electrothermal treatment is identified as an important next step, particularly for Sn-rich compositions where elevated local temperatures may accelerate Sn^{2+} oxidation.

The resulting far-field emission patterns and optical enhancement metrics are analyzed in Section 3 to establish composition–structure–performance relationships.

3. Results and discussion

3.1. Electrical and optical properties of $CsSn_xGe_{1-x}I_3$

The structural, electronic, and optical properties of $CsSn_xGe_{1-x}I_3$ ($0 \leq x \leq 1$) were systematically investigated using density functional theory (DFT) to establish the

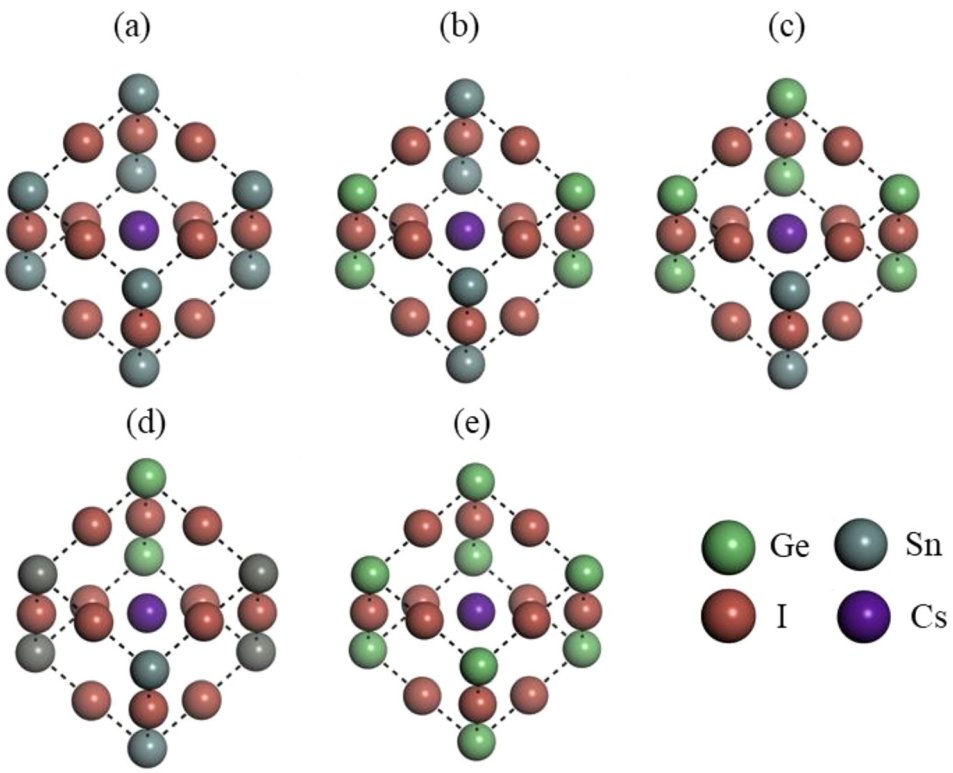

Fig. 4 Different doping arrangements of $CsSn_xGe_{1-x}I_3$. (a) $x = 1$, (b) $x = 0.75$, (c) $x = 0.5$, (d) $x = 0.25$ and (e) $x = 0$. Green, grey, brown, and violet indicate Ge, Sn, I, and Cs, respectively.

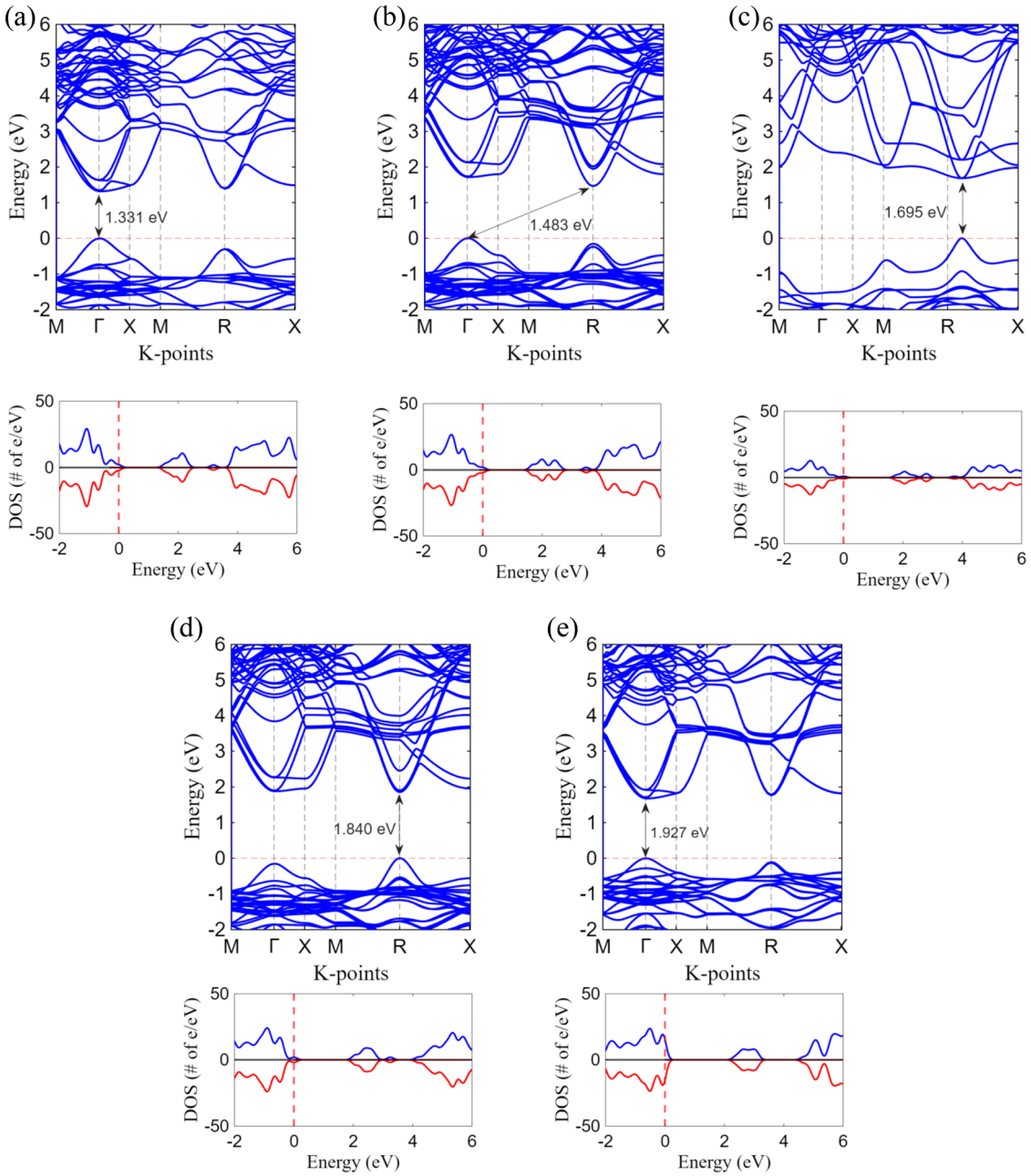

Fig. 5 Electronic band structures and the corresponding total density of states (DOS) of (a) $CsSnI_3$, (b) $CsSn_{0.75}Ge_{0.25}I_3$, (c) $CsSn_{0.5}Ge_{0.5}I_3$, (d) $CsSn_{0.25}Ge_{0.75}I_3$, and (e) $CsGeI_3$ along the high-symmetry k-path (M–Γ–X–M–R–X). The Fermi level is set to 0 eV (red dashed line). The calculated band gaps are 1.331 eV, 1.483 eV, 1.695 eV, 1.840 eV, and 1.927 eV with increasing Ge composition, respectively. A systematic widening of the band gap is observed across the $CuSn_xGe_{1-x}I_3$ series. The DOS plots further confirm the semiconducting nature of all compositions, showing negligible states at the Fermi level and gradual shifts of the valence and conduction band edges upon Ge substitution.

composition–property relationships governing light emission and plasmonic interactions in PeLED architectures. Five representative alloy configurations, pure $CsSnI_3$ (x = 1), $CsSn_{0.75}Ge_{0.25}I_3$, $CsSn_{0.5}Ge_{0.5}I_3$, $CsSn_{0.25}Ge_{0.75}I_3$, and pure $CsGeI_3$ (x = 0), were analyzed to understand the effect of doping gradually (Fig. 4). All structures converged to the orthorhombic perovskite phase, maintaining a corner-sharing octahedral structure. The lattice volume decreased monotonically with increasing Ge content, consistent with the smaller ionic radius of Ge^{2+} relative to Sn^{2+}. This contraction leads to stronger metal–halide orbital overlap and influences both band dispersion and optical transition strength.

Fig. 5 shows the calculated electronic band structures and total density of states (DOS) of $CsSn_xGe_{1-x}I_3$ for varying Ge compositions. All compounds exhibit semiconducting behavior with a clear band gap at the Fermi level. The band gap increases systematically from 1.331 eV for $CsSnI_3$ to 1.927 eV for $CsGeI_3$, indicating effective band-gap tuning through Ge substitution.

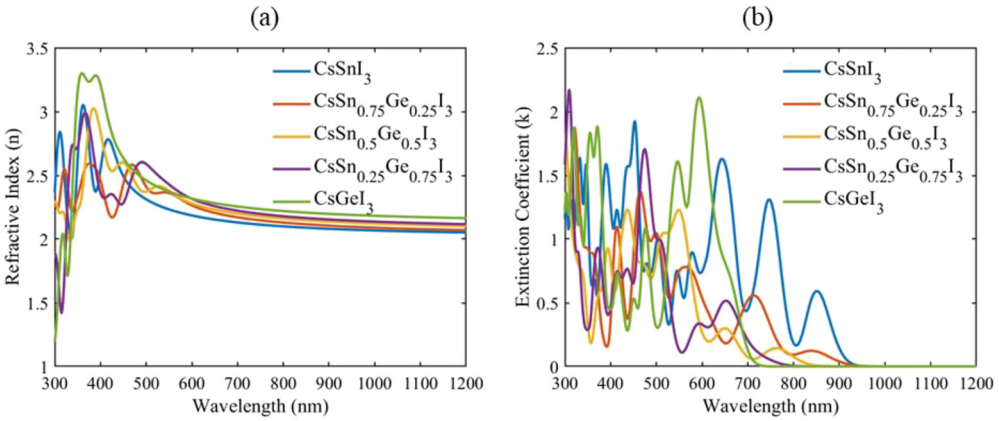

Fig. 6 Optical properties of $CsSn_xGe_{1-x}I_3$: (a) refractive index and (b) extinction coefficient for various compositions of x.

The DOS profiles further confirm the absence of states at the Fermi level and reveal gradual shifts in the valence and conduction band edges with increasing Ge content.

The absorption coefficient can be derived from the complex dielectric constant, $\varepsilon = \varepsilon_1 + i\varepsilon_2$. The imaginary part ($\varepsilon_2$) of the dielectric constant (ε) can be calculated using the following formula from the electrical band structure[56]:

$$\varepsilon_2(q \to 0_{\hat{u}}, \hbar\omega) = \frac{2e^2\pi}{\Omega\varepsilon_0}\sum_{k,v,c}\left|\left\langle \Psi_k^c|\mathbf{u}\cdot\mathbf{r}|\Psi_k^v\right\rangle\right|^2\delta\left(E_k^c - E_k^v - \hbar\omega\right) \quad (1)$$

where $\mathbf{u}$ is the vector defining the polarization of the incident light, $\left\langle \Psi_k^c|\mathbf{u}\cdot\mathbf{r}|\Psi_k^v\right\rangle$ is the matrix element, E_k^c is the conduction band energy, E_k^v is the valence band energy at wave number k, ω is the angular frequency of the electron, e is the charge, $\mathbf{u}\cdot\mathbf{r}$ is the momentum operator, and $\hbar$ is the reduced Planck's constant. The real part of the dielectric constant can be found using the Kramers–Kronig transformation:[57]

$$\varepsilon_1(\omega) = 1 + \frac{2}{\pi}P\int_0^\infty \frac{\varepsilon_2(\omega^*)\omega^*}{\omega^{*2} - \omega^2}\mathrm{d}\omega^* \quad (2)$$

where P is the principal value of the integral. The optical absorption coefficient for the material is calculated as a function of the dielectric constant as follows:[58]

$$\alpha(\omega) = \frac{4\pi k(\omega)}{\lambda\sqrt{2}}\left(\sqrt{\varepsilon_1^2(\omega) + \varepsilon_2^2(\omega)} - \varepsilon_1(\omega)\right)^{1/2} \quad (3)$$

where ε_1 and ε_2 are the real and imaginary parts of the dielectric function, k is the extinction coefficient, and λ is the wavelength. The refractive index (n) and extinction coefficient (k) can be obtained from the dielectric constant using the following formulas:[59]

$$n(\omega) = \frac{1}{\sqrt{2}}\left[\sqrt{\varepsilon_1^2(\omega) + \varepsilon_2^2(\omega)} + \varepsilon_1(\omega)\right]^{1/2} \quad (4)$$

$$k(\omega) = \frac{1}{\sqrt{2}}\left[\sqrt{\varepsilon_1^2(\omega) + \varepsilon_2^2(\omega)} - \varepsilon_1(\omega)\right]^{1/2} \quad (5)$$

The complex refractive index (n and k spectra) obtained from the frequency-dependent dielectric function reveals pronounced compositional dependence (Fig. 6). The optical constants were calculated within the independent-particle DFT framework; although excitonic effects were not explicitly included, their influence is expected to cause only minor quantitative shifts near the band edge without affecting the overall spectral trends used in the FDTD simulations.

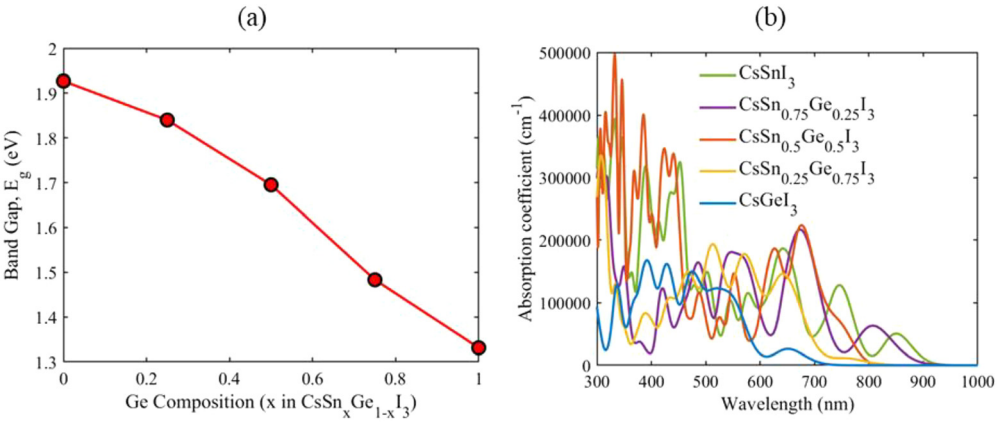

Fig. 7 (a) Bandgap of $CsSn_xGe_{1-x}I_3$ for various compositions of x. (b) Absorption coefficient of $CsSn_xGe_{1-x}I_3$ for various compositions of x.

Increasing Ge substitution systematically blueshifts the $n(\lambda)$ and $k(\lambda)$ spectra, reflecting the widening electronic bandgap. Importantly, the magnitude of n remains high ($\sim$2.2–2.6 in the visible/NIR region), corroborating the inherently strong light-confinement characteristics of Sn/Ge-based perovskites and explaining the limited intrinsic light extraction efficiency in planar PeLEDs.

The absorption coefficients in Fig. 7(b) further confirm the influence of Ge incorporation on optical transitions. Pure $CsSnI_3$ exhibits strong absorption extending into the NIR region, whereas Ge-rich compositions shift the absorption edge toward shorter wavelengths, consistent with increased bandgap energies. The absorption amplitude remains high ($>10^5$ cm^{-1} across the visible–NIR window), reaffirming the exceptional oscillator strength and suitability of these materials for high-radiance emitter applications. Alloy compositions (x = 0.25–0.75) show intermediate absorption edges, enabling fine-tuning of emission wavelengths for targeted plasmonic coupling with Au nanorods.

The electronic bandgap analysis of the DFT optical spectra displays a nearly linear dependence on alloy composition (Fig. 7a). $CsSnI_3$ shows the smallest bandgap of 1.331 eV, while $CsGeI_3$ exhibits a significantly larger value of 1.927 eV, with mixed alloys occupying the intermediate range. Ge substitution reduces the antibonding interaction strength in the metal–iodide network, widening the bandgap and shifting emission toward shorter wavelengths. Such tunability is crucial because it enables precise matching of the emissive peak with the longitudinal plasmon resonance of Au/SiO_2 nanorods for maximized Purcell enhancement. While direct LED emission data for intermediate $CsSn_xGe_{1-x}I_3$ compositions remain limited, prior experimental and theoretical studies confirm monotonic bandgap widening with increasing Ge incorporation.[18,27,30] The calculated bandgap of $CsGeI_3$ (1.927 eV) agrees well with reported literature values near 1.9 eV.[30] Together with the excellent agreement between our predicted $CsSnI_3$ emission (931 nm) and experimentally reported values (930–950 nm),[24–26] this consistency for both end members supports the reliability of the predicted intermediate alloy behavior.

The DFT results establish a clear composition-dependent evolution of lattice structure, bandgap, and optical constants in

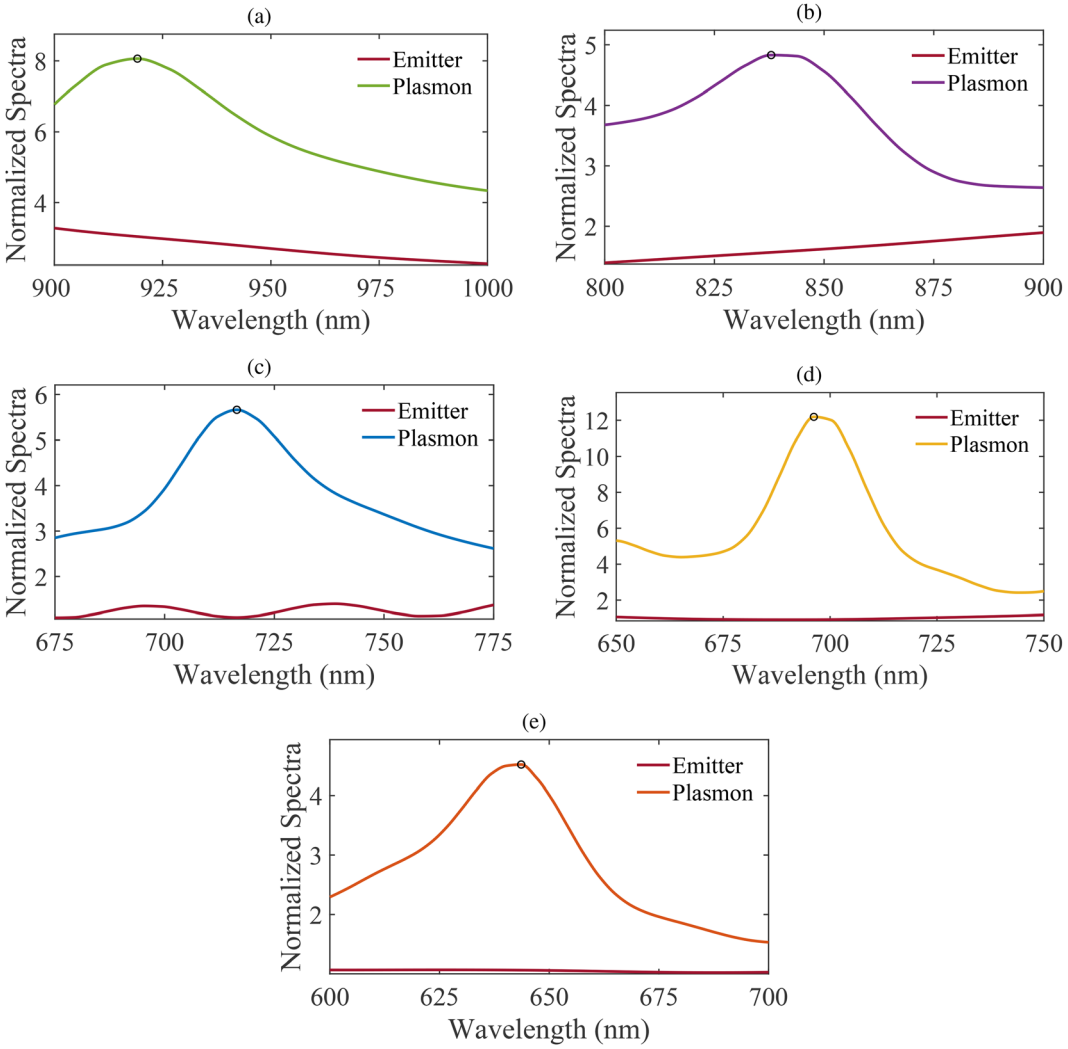

Fig. 8 Composition-dependent Purcell factor enhancement in $CsSn_xGe_{1-x}I_3$-based LEDs for (a) x = 1, (b) x = 0.75, (c) x = 0.5, (d) x = 0.25, and (e) x = 0.

$CsSn_xGe_{1-x}I_3$. These properties constitute the fundamental inputs for the subsequent FDTD modeling.

3.2. FDTD results

3.2.1. Purcell factor enhancement. The Purcell factor is a measure of the enhancement of an emitter's spontaneous decay rate when nanostructures are placed nearby.[62] This enhancement occurs due to the modification of local photonic density of states (LDOS) at the emitter. The Purcell factor enhancement of the LED is shown in Fig. 8 for all values of x. Black markers indicate the peak values of Purcell across all x values. The highest Purcell factor of 12 was achieved for $CsSn_{0.25}Ge_{0.75}I_3$ for a NR length of 60 nm and a radius of 11 nm. This indicates strong coupling between the emitter and the

Table 1 Comparison of the calculated band gaps (this work) with reported values (Ref.) and the corresponding FDTD simulation results of $CsSn_xGe_{1-x}I_3$ nanorod emitters

	Bandgap (eV)		Emission	NR size (nm)		Purcell		LEE (%)		Sp. Ovlp.
Composition	This work	Ref.	λ (nm)	Length	Radius	Peak	λ (nm)	Value	Enh.	J_{cos}
$CsGeI_3$	1.927	1.90[30]	643	55	11	4.4	643	24.9	17	0.89
$CsSn_{0.25}Ge_{0.75}I_3$	1.840	1.84[60]	674	60	11	12.1	695	19	34	0.80
$CsSn_{0.5}Ge_{0.5}I_3$	1.695	1.69[60]	731	70	17	5.3	721	25	33	0.93
$CsSn_{0.75}Ge_{0.25}I_3$	1.483	1.48[60]	836	120	17	4.9	837	23	28	0.96
$CsSnI_3$	1.331	1.30[61]	931	170	19	8.0	928	17.5	36	0.96

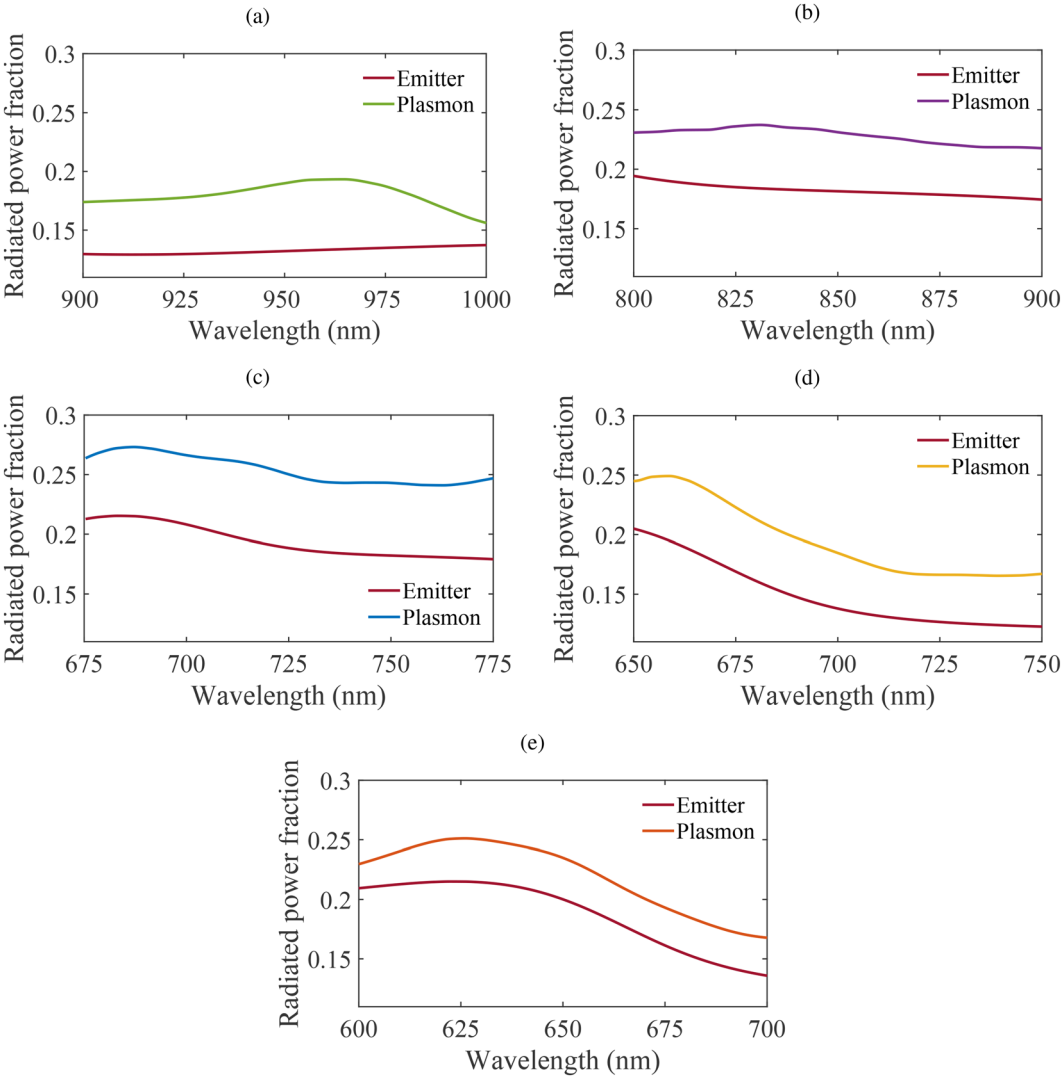

Fig. 9 Composition-dependent LEE in $CsSn_xGe_{1-x}I_3$-based LEDs for (a) x = 1, (b) x = 0.75, (c) x = 0.5, (d) x = 0.25, and (e) x = 0.

plasmonic nanostructure. Table 1 shows the Purcell enhancement for all $CsSn_xGe_{1-x}I_3$ compositions and the corresponding NR length and radius values.

Coincidence of the plasmon spectrum peak with the emitter peak creates resonance, increasing LDOS at that wavelength. This resonant condition in turn enhances the radiative decay rate of the emitter resulting in a large Purcell factor.[63] Under other conditions where the plasmonic response is weaker or not in coincidence with the emitter peak, LDOS may still be increased due to scattering.[64] This is responsible for Purcell enhancements that are not sharp. The measured Purcell behavior is a superposition of both resonance-driven enhancement, where spectral overlap is significant, and broadband off-resonant LDOS perturbation, where overlap is negligible.[63]

3.2.2. LEE and LEE enhancement. The light extraction efficiency (LEE) quantifies the fraction of generated photons that escape the device structure.[65] Without plasmonic nanorods, the baseline LEE for these high-index perovskites is approximately 8%. Fig. 9 and 10 show the composition-dependent LEE in $CsSn_xGe_{1-x}I_3$-based LEDs. It can be seen that LEE consistently increases with Ge content, reaching a maximum of 25% for $CsSn_{0.5}Ge_{0.5}I_3$ using a NR length of 70 nm and a radius of 17 nm. The highest LEE enhancement of 36% was obtained for $CsSnI_3$ ($x = 1$) using a NR length of 170 nm and a radius of 19 nm.

Several mechanisms work in synergy when Au NRs are used for LEE and LEE enhancement. When NRs are placed near the perovskite emitter, they support localized surface plasmon resonance (LSPR), opening additional radiative channels and enhancing the local density of optical states.[66] The presence of NR breaks the symmetry of the device stack, scattering previously trapped waveguide modes into the far field and adding directionality to the emission.[67] This scattering contribution, combined with the Purcell-driven increase in radiative photon generation, increases the fraction of photons that escape the structure.[66] NR geometry also allows precise resonance tuning and large scattering cross-sections, further boosting both LEE and LEE enhancement across compositions.

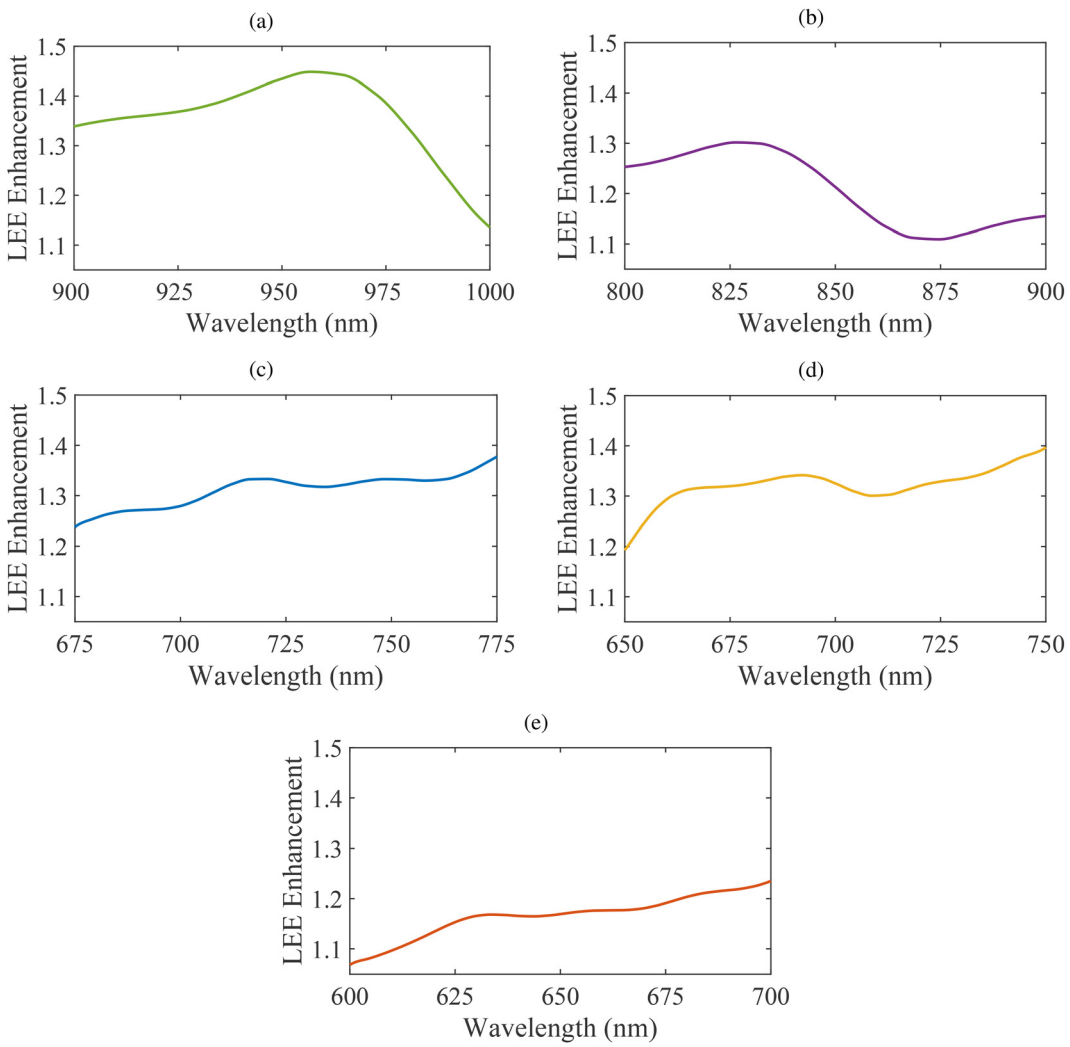

Fig. 10 Composition-dependent LEE enhancement in $CsSn_xGe_{1-x}I_3$-based LEDs for (a) $x = 1$, (b) $x = 0.75$, (c) $x = 0.5$, (d) $x = 0.25$, and (e) $x = 0$.

Table 1 shows the achieved LEE and LEE enhancement values for all compositions along with the corresponding NR length and radius values. It is important to note that although plasmonic coupling enhances the spontaneous emission rate (Purcell factor), not all enhanced emission contributes to far-field radiation. The gap between Purcell enhancement and LEE indicates that a portion of the optical energy remains confined within the structure or is dissipated through metallic absorption. The present work focuses on radiative outcoupling trends across compositions, while a rigorous separation of individual loss channels (*e.g.*, SPP modes *versus* waveguide modes) is identified as an important direction for future work.

3.2.3. Spectral overlap analysis. Spectral overlap presents the amount of alignment of the plasmon resonance spectrum with the emitter's photoluminescence spectrum.[68] Transverse mode LSPR is used, which can be effective for spectral overlap alignment in perovskites having refractive index $n \approx 2.0$–2.6. Composition-dependent LEE and LEE enhancement values for all values of x in $CsSn_xGe_{1-x}I_3$ are shown in Fig. 11. The highest spectral overlap (J_{cos}) of about 96% has been achieved for both $CsSn_{0.75}Ge_{0.25}I_3$ and $CsSnI_3$ at the peak Purcell wavelength. J_{cos} is defined by[69]

$$J = \int S_{emit}(\lambda) C_{plasmon}(\lambda) d\lambda \quad (6)$$

$$J_{cos} = \frac{\int S(\lambda) C(\lambda) d\lambda}{\sqrt{\int S^2(\lambda) d\lambda} \sqrt{\int C^2(\lambda) d\lambda}} \quad (7)$$

The achieved J_{cos} values for all compositions of $CsSn_xGe_{1-x}I_3$ and the corresponding NR length and radius values are shown in Table 1.

The refractive index of perovskites influences the LSPR spectral position due to changes in the dielectric environment, enabling resonance tuning by the design of the nanostructure geometry.[70] This also helps in broadening the plasmon spectrum, thus covering a larger portion of the emitter spectrum and increasing overlap. Plasmons can boost emission where the perovskite spectrum falls off. This increases overlap even if the peaks are not perfectly aligned.[71] The presence of vertical

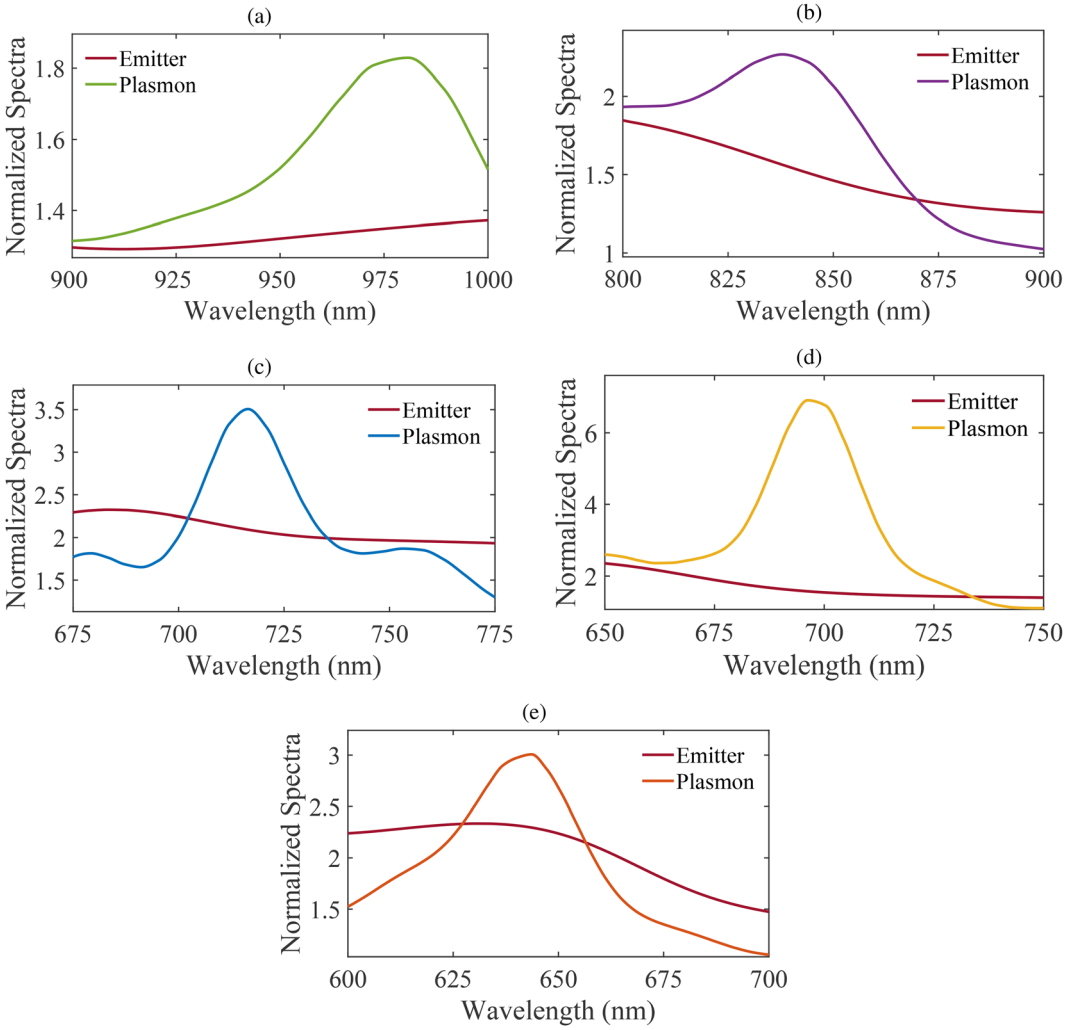

Fig. 11 Composition-dependent spectral overlap in $CsSn_xGe_{1-x}I_3$-based LEDs for (a) $x = 1$, (b) $x = 0.75$, (c) $x = 0.5$, (d) $x = 0.25$, and (e) $x = 0$.

scattering channels also increases radiative contribution in the transverse mode.[72]

3.2.4. Far-field emission profiles. Far-field plots depict the amount of light escaping the LED and radiating outward as freely propagating radiation.[73] Previously discussed mechanisms such as the enhancement of near-field to far-field conversion through plasmonic scattering, Purcell-enhanced radiative decay, symmetry breaking of waveguide modes, and transverse LSPR act together to provide strong far-field emission profiles.

Composition-dependent far-field plots for all values of x in $CsSn_xGe_{1-x}I_3$ are shown in Fig. 12. Sn-rich (x = 1) compositions emit in the deeper NIR region. Here the transverse LSPR scatters weakly, resulting in a dimmer far-field pattern. But as the Ge content increases, the emission shifts to shorter wavelengths. This blue shift is caused by the bandgap widening due to Ge alloying. These wavelengths couple more strongly to the Au NR resonance, producing stronger scattering and a brighter far-field map. So, the far-field intensity increases steadily with increasing Ge fraction in $CsSn_xGe_{1-x}I_3$ based LEDs.

Fig. 13a presents the angular line cuts extracted from the far-field emission maps for all $CsSn_xGe_{1-x}I_3$ compositions. The emission profiles exhibit strong composition dependence with Ge-rich alloys showing relatively narrow angular distributions. Sn-rich compositions display significantly broadened emission. This broadening is attributed to the higher refractive index of Sn-rich perovskites. This enhancement redistributes radiative power over wider emission angles.

Fig. 13b summarizes the angular emission characteristics using the FWHM of the angular profiles. The FWHM increases with Sn content. This confirms the transition from directional emission in Ge-rich compositions to more diffuse radiation in Sn-rich alloys.

To quantify the total radiative output, the far-field intensity was integrated over all emission angles (Fig. 13c). The integrated power exhibits a non-monotonic dependence on composition, reaching a maximum near x = 0.5. This indicates that optimal far-field extraction does not coincide with the strongest Purcell enhancement but instead arises from a balance between emission rate enhancement and angular outcoupling.

3.3. Comparison with reported PeLED architectures

To place the performance of the $CsSn_xGe_{1-x}I_3$-based PeLEDs in context, Table 2 compares the Purcell factor and LEE reported for perovskite LED architectures published between 2021 and 2025. The table focuses mainly on lead-free and reduced-lead systems. Lead-based $CsPbBr_3$ devices are included only as reference benchmarks. Many earlier studies improve either the emission rate or the optical outcoupling, but not both at the same time. Clear and combined reporting of Purcell enhancement and LEE is still uncommon, especially for lead-free emitters.

As shown in Table 2, this work is among the few studies that quantitatively evaluate both Purcell enhancement and LEE within a single lead-free device platform. When compared with $CsPbBr_3$ microcavity and resonator benchmarks, the

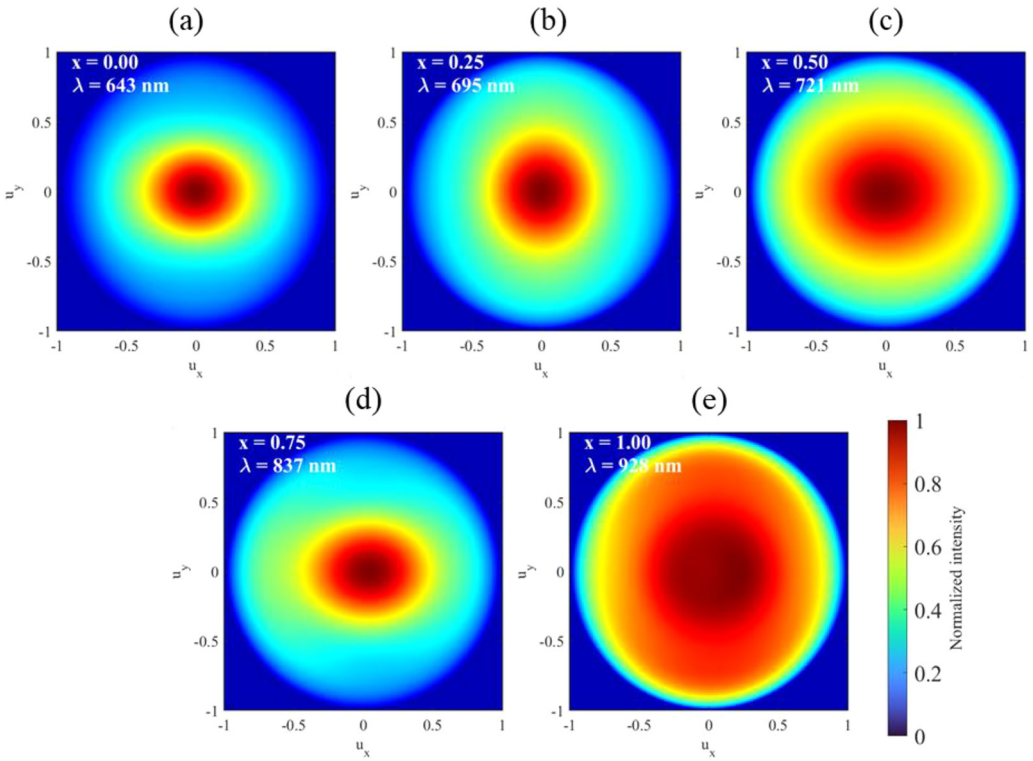

Fig. 12 Far-field emission profiles of $CsSn_xGe_{1-x}I_3$-based LEDs for (a) x = 1, (b) x = 0.75, (c) x = 0.5, (d) x = 0.25, and (e) x = 0. The common color scale corresponding to the normalized far-field intensity used for all compositions.

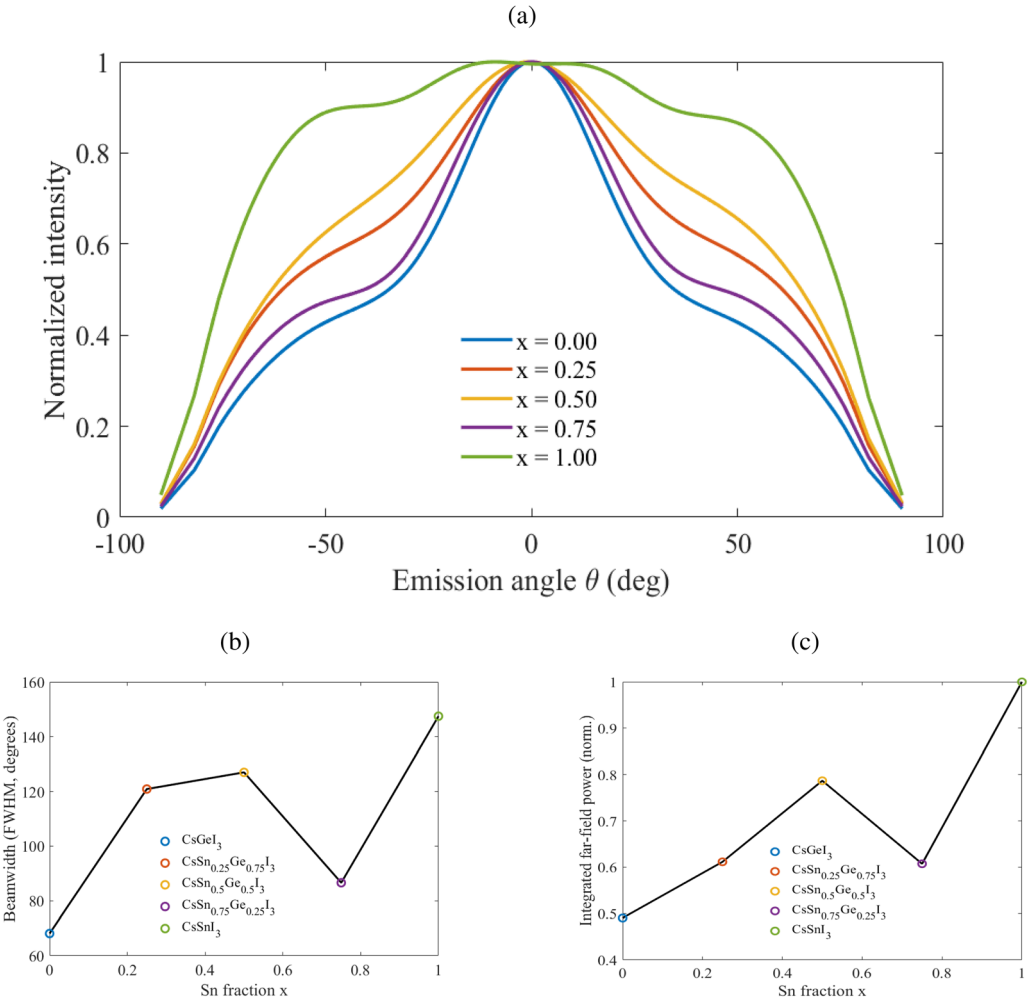

Fig. 13 Far-field emission analysis of $CsSn_xGe_{1-x}I_3$-based LEDs. (a) Angular line cuts extracted from the far-field emission maps, illustrating composition-dependent emission directionality. (b) Beam width (FWHM) of the angular emission profiles, quantifying the transition from directional to diffuse emission with increasing Sn content. (c) Integrated far-field radiated power as a function of Sn composition, highlighting a non-monotonic extraction trend.

Table 2 Comparison of the Purcell factor and light extraction efficiency (LEE) in perovskite LEDs reported between 2021 and 2025

Emitting material	Emission (nm)	Purcell factor	LEE/outcoupling	Optical structure	Methodology	Ref.
$CsSn_{0.25}Ge_{0.75}I_3$ (this work)	~670	12× (sim.)	~19%	Au/SiO_2 nanorods	DFT n,k + FDTD	This work
$CsSn_{0.5}Ge_{0.5}I_3$ (this work)	~730	5.3× (sim.)	25%	Au/SiO_2 nanorods	FDTD, near–far field	This work
$FASnI_3$	~880	PF inferred	Grating-assisted	DFB grating	Exp. + mode analysis	74
$Cs_2AgBiBr_6$	NIR	—	~42% (sim.)	Metal microcavity	FDTD	39
$Cs_3Cu_2I_5$	~440	Implicit	Directional	VCSEL cavity	Experiment	75
$CsPbBr_3$ (bench.)	~530	~2–3×	31–38%	Planar microcavity	TMM + dipole	76
$CsPbBr_3$ (bench.)	~520	~2×	~18×	Mie resonator	FDTD + TRPL	77

Lead-based $CsPbBr_3$ devices are included only as benchmarks

$CsSn_{0.5}Ge_{0.5}I_3$ composition shows competitive light extraction. At the same time, it maintains strong emission-rate enhancement. These results highlight the benefit of using composition-aware plasmonic design to balance light generation and light extraction.

3.4. Design considerations

The best Purcell factor does not necessarily lead to the best light extraction. This is due to a clear tradeoff between near-field enhancement and outcoupling. At $x = 0.25$, the emitter spectrum and the plasmon resonance are almost perfectly aligned. This strong match accelerates photon generation and drives the Purcell factor up to about 12×. The drawback is that this composition has a relatively high refractive index of roughly 2.5, which traps much of the emitted light inside the device.

At $x = 0.5$, the spectral match is slightly weaker, but the lower refractive index reduces total internal reflection, allowing more

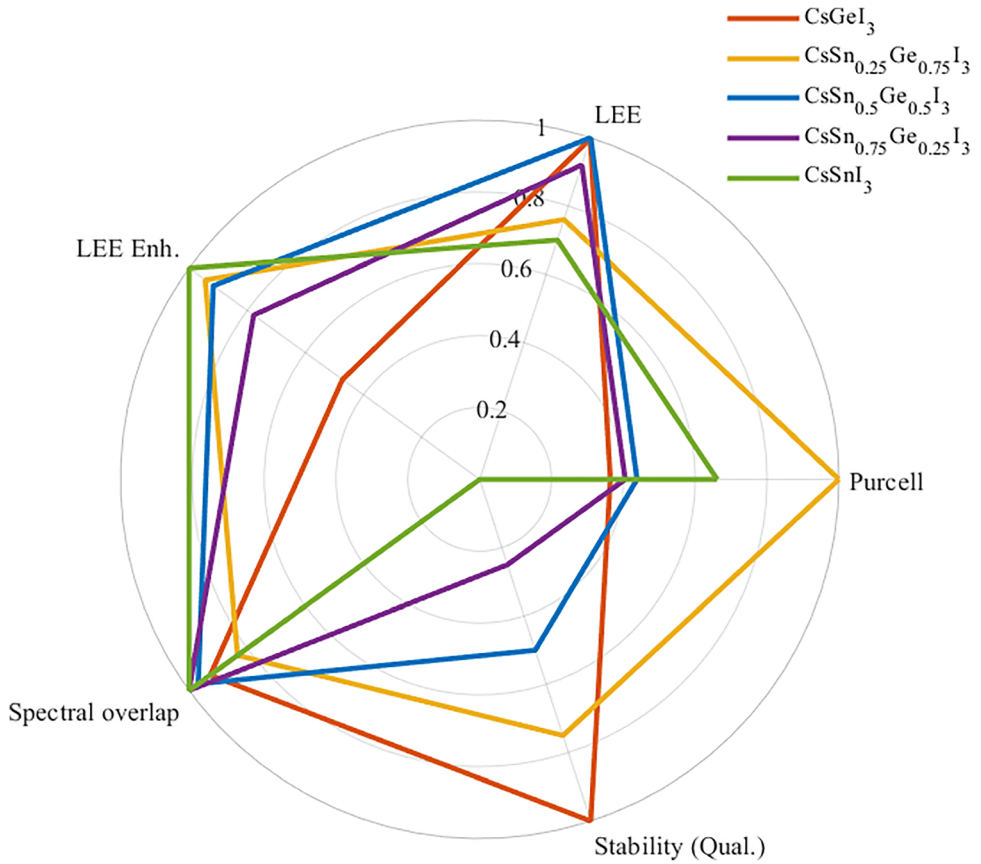

Fig. 14 Spider plot comparing the normalized performance metrics of $CsSn_xGe_{1-x}I_3$ PeLEDs, including the Purcell factor, LEE, LEE enhancement, spectral overlap, and compositional stability. Compositional stability is represented using the Ge fraction $(1 - x)$ as a qualitative proxy.

photons to escape. In practice, this means that $x = 0.25$ is more efficient at producing light, while $x = 0.5$ is more efficient at releasing it. This distinction shows that Purcell enhancement and far-field extraction should be treated as two separate but equally important design factors. Simply increasing the spontaneous emission rate does not automatically lead to the best overall device performance.

These trends also guide the choice of nanorod geometry. Sn-rich compositions emit farther into the NIR region and therefore couple best to longer nanorods of about 170 nm, which match the red-shifted plasmon resonance. Ge-rich compositions emit at shorter wavelengths and achieve stronger coupling with shorter nanorods in the range of 55 to 70 nm.

These competing effects are summarized in Fig. 14, which compares Purcell enhancement, spectral overlap, light extraction efficiency, and LEE enhancement across compositions. To provide contextual design guidance, compositional stability is represented qualitatively using the Ge fraction $(1 - x)$ as a literature-supported indicator of improved oxidation resistance. Previous experimental studies have reported enhanced environmental stability in Sn–Ge mixed perovskites due to the formation of native GeO_x surface passivation layers.[30] However, it should be emphasized that no defect formation energy calculations or thermodynamic stability modeling were performed in the present work. The stability axis in Fig. 14 (labeled "Stability (Qual.)") therefore serves only as a conceptual design parameter rather than a quantitatively computed metric.

While Fig. 14 highlights discrete composition-dependent trends, the underlying tradeoffs can be more clearly visualized using continuous design maps. Fig. 15 presents two-dimensional landscapes that show how Purcell enhancement, light extraction, and spectral overlap evolve simultaneously with composition, emission wavelength, and plasmonic geometry. These maps complement the spider plot by revealing optimal design regions rather than isolated operating points.

3.5. Experimental validation and fabrication outlook

To validate our computational methodology, we compare our predictions for $CsSnI_3$ with recent experimental demonstrations. Our DFT calculations predict an emission wavelength of 931 nm for $CsSnI_3$, showing excellent agreement with experimentally measured values of 930–950 nm.[24–26] This confirms the accuracy of our DFT-derived optical constants.

Recent breakthroughs have demonstrated $CsSnI_3$ NIR PeLEDs with external quantum efficiencies of 7.6%,[24] a peak radiance of 226 W sr^{-1} m^{-2}, and operational lifetimes exceeding 39 hours at 100 mA cm^{-2}.[25] These results confirm that Sn-based perovskites can function effectively as LED emitters.

Although mixed Sn–Ge compositions have not yet been extensively demonstrated in LED architectures, their successful

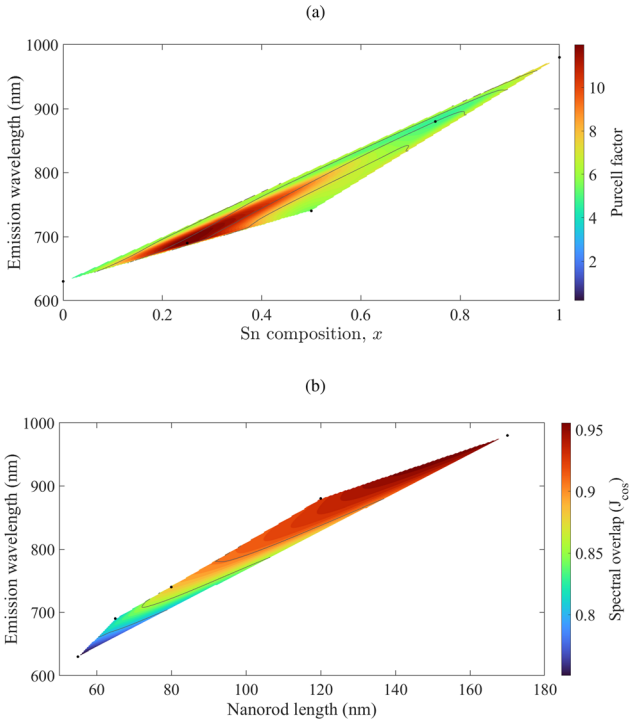

Fig. 15 Design landscapes illustrating competing emission and extraction mechanisms in $CsSn_xGe_{1-x}I_3$ PeLEDs. (a) Purcell–LEE tradeoff map as a function of Sn composition, x, and emission wavelength, where the color scale denotes the Purcell factor and contour lines indicate regions of comparable light extraction efficiency. (b) Spectral overlap landscape (J_{cos}) between the emitter spectrum and plasmonic resonance as a function of nanorod length and emission wavelength, showing a systematic shift of optimal overlap toward longer nanorods for Sn-rich compositions.

synthesis and optical characterization in photovoltaic systems[30] confirm the structural feasibility and smooth compositional evolution of $CsSn_xGe_{1-x}I_3$ alloys. The present study therefore provides experimentally testable emission and plasmonic design targets for future realization of mixed Sn–Ge PeLEDs. Our framework specifically predicts optimal performance for $CsSn_{0.5}Ge_{0.5}I_3$ at an emission wavelength of 721 nm, utilizing Au/SiO_2 nanorods with a length of 70 nm and a radius of 17 nm.

Solution processability of both pure Sn[24] and mixed Sn–Ge[30] perovskites, along with established plasmonic nanoparticle integration methods,[41] indicates experimental realization is feasible. Key considerations include anti-solvent treatment optimization, SnF_2 additives for oxidation suppression, and nanorod positioning control.

4. Conclusion

We have established a DFT–FDTD computational framework to design plasmon-enhanced lead-free $CsSnI_3$ perovskite LEDs. DFT calculations provided accurate optical constants for five compositions (x = 0, 0.25, 0.5, 0.75, and 1). Our predicted emission wavelength for $CsSnI_3$ is 931 nm. This shows excellent agreement with recent experimental demonstrations at 930–950 nm and validates our methodology.

Among all tested compositions, $CsSn_{0.5}Ge_{0.5}I_3$ delivers the most balanced performance. It achieves the highest light extraction efficiency (25%), strong Purcell enhancement (5.3×), and 93% spectral overlap. Improved oxidation resistance has been reported in prior experimental studies of Sn–Ge mixed perovskites.[30] It should be noted that the stability trends discussed here are literature-informed and were not directly calculated within the present framework. The results also suggest that longer nanorods suit Sn-rich NIR emitters, while shorter nanorods suit Ge-rich visible emitters.

The reported efficiencies are derived from far-field radiative power and do not explicitly decompose confined or absorptive loss channels. These simulations also do not account for non-radiative recombination or defect-induced quenching effects common in Sn-based perovskites. Thus, the calculated Purcell enhancement and LEE represent optical upper bounds assuming high internal quantum efficiency. Actual experimental device performance may be lower, depending heavily on defect passivation quality and recombination dynamics. Plasmonic enhancement inherently involves a trade-off between radiative rate enhancement and ohmic absorption losses in metallic nanostructures. Careful optimization of spacer thickness is necessary to suppress quenching in experimental realizations. Coupled electrothermal modeling of heat dissipation in the Au nanorod, beyond the scope of the present optical study, will be important for assessing device reliability in future work. Building on the successful experimental demonstration of $CsSnI_3$ LEDs, our validated computational framework provides systematic design guidelines for optimizing the full $CsSn_xGe_{1-x}I_3$ compositional range.

The combination of tunable emission wavelengths (643–931 nm), strong plasmonic response, and Ge-induced stability makes $CsSn_xGe_{1-x}I_3$ promising lead-free candidates for next-generation flexible and wearable optoelectronics. Experimental validation of these predictions through fabrication and characterization of mixed Sn–Ge LED devices is the logical next step.

Conflicts of interest

The authors declare no conflicts of interest.

Data availability

Representative finite-difference time-domain (FDTD) simulation files supporting this study are available at the following GitHub repository: https://github.com/debnath-shoumik/PeLED_FDTD_CsSnxGe1xI3.

Additional data may be obtained from the corresponding author upon reasonable request.

Acknowledgements

The authors acknowledge the financial support from the Basic Research Grant, Bangladesh University of Engineering and

Technology (BUET), under Office Order No. Shongstha/R-60/Re-2413, dated 10 October 2023 (Professor Dr Md. Zahurul Islam). The authors also acknowledge the logistical support provided by the Department of Electrical and Electronic Engineering (EEE), BUET, throughout this work.

References

1 C. Cho, Y. Sun, J. You, L. S. Cui and N. C. Greenham, Enhanced Photon Recycling Enables Efficient Perovskite Light-Emitting Diodes, *Adv. Funct. Mater.*, 2024, **34**(49), 2411556.
2 Y. Liu, Z. Ma, J. Zhang, Y. He, J. Dai and X. Li, *et al.*, Light-Emitting Diodes Based on Metal Halide Perovskite and Perovskite Related Nanocrystals, *Adv. Mater.*, 2025, **37**, 2415606.
3 A. Rogalski, F. Wang, J. Wang, P. Martyniuk and W. Hu, The Perovskite Optoelectronic Devices - A Look at the Future, *Small Methods*, 2025, **9**, 2400709.
4 Z. Chen, R. L. Z. Hoye and H. L. Yip, *et al.*, Roadmap on perovskite light-emitting diodes, *J. Phys.: Photonics*, 2024, **6**(3), 032501.
5 P. Xiong, J. B. Liao, Z. Y. Wang, Q. H. Zuo, Y. Dai and J. Wu, *et al.*, First-principles study on electronic and optical properties of perovskite light-emitting diodes CsPb(Br1-xIx)3, *Appl. Phys. Lett.*, 2025, **126**(2), 023911.
6 F. Lu, Y. Liang, N. Wang, L. Zhu and J. Wang, Machine learning for perovskite optoelectronics: A review, *Adv. Photonics*, 2024, **6**, 054001.
7 J. Sanchez-Diaz, J. Rodriguez-Pereira, S. Das Adhikari and I. Mora-Seró, Synthesis of Hybrid Tin-Based Perovskite Microcrystals for LED Applications, *Adv. Sci.*, 2024, **11**(34), 2403835.
8 L. Kong, Y. Sun, B. Zhao, K. Ji, J. Feng and J. Dong, *et al.*, Fabrication of red-emitting perovskite LEDs by stabilizing their octahedral structure, *Nature*, 2024, **631**(8019), 73–79.
9 C. C. Li, T. Y. Huang, Y. H. Lai, Y. C. Huang and C. S. Tan, Lead-free perovskites for flexible optoelectronics, *Mater. Today Electron.*, 2024, **8**, 100095.
10 Y. Nong, J. Yao, J. Li, L. Xu, Z. Yang and C. Li, *et al.*, Boosting External Quantum Efficiency of Blue Perovskite QLEDs Exceeding 23% by Trifluoroacetate Passivation and Mixed Hole Transportation Design, *Adv. Mater.*, 2024, **36**(27), 2402325.
11 C. Ma, M. Ni, X. Liu, K. Zhan, M. Chen and S. Li, *et al.*, Recent progress in perovskite light-emitting diodes with high external quantum efficiency and stability, *CrystEngComm*, 2025, **27**, 3853–3876.
12 Y. Xiao, Q. Xue, X. Liu, F. Gao and G. Xie, Lead-free perovskite LEDs powered by cyanuric acid, *The Innovation*, 2024, **5**, 100553.
13 Q. Dong, L. Lei, J. Mendes and F. So, Operational stability of perovskite light emitting diodes, *J. Phys.: Energy*, 2020, **3**, 012002.
14 D. Yang, B. Zhao, T. Yang, R. Lai, D. Lan and R. H. Friend, *et al.*, Toward Stable and Efficient Perovskite Light-Emitting Diodes, *Adv. Funct. Mater.*, 2022, **32**, 2109495.
15 S. Liu, Y. Wu, J. Wu and Z. Lin, Blue Emission from Metal Halide Perovskites: Strategies and Applications, *ChemPhotoChem*, 2024, **8**, e202400139.
16 P. K. Ko, J. Ge, P. Ding, D. Chen, H. L. T. Tsang and N. Kumar, *et al.*, The Deepest Blue: Major Advances and Challenges in Deep Blue Emitting Quasi-2D and Nanocrystalline Perovskite LEDs, *Adv. Mater.*, 2025, **37**, 2407764.
17 M. Li, Y. Yang, Z. Kuang, C. Hao, S. Wang and F. Lu, *et al.*, Acceleration of radiative recombination for efficient perovskite LEDs, *Nature*, 2024, **630**(8017), 631–635.
18 I. López-Fernández, D. Valli and C. Y. Wang, *et al.*, Lead-Free Halide Perovskite Materials and Optoelectronic Devices: Progress and Prospective, *Adv. Funct. Mater.*, 2024, **34**, 2307896.
19 L. Zhang, C. Sun, T. He, Y. Jiang, J. Wei and Y. Huang, *et al.*, High-performance quasi-2D perovskite light-emitting diodes: from materials to devices, *Light: Sci. Appl.*, 2021, **10**, 66.
20 J. Chen, H. Xiang, J. Wang, R. Wang, Y. Li and Q. Shan, *et al.*, Perovskite White Light Emitting Diodes: Progress, Challenges, and Opportunities, *ACS Nano*, 2021, **15**, 17150–17174.
21 S. Kar, N. F. Jamaludin, N. Yantara, S. G. Mhaisalkar and W. L. Leong, Recent advancements and perspectives on light management and high performance in perovskite light-emitting diodes, *Nanophotonics*, 2021, **10**, 2103–2143.
22 M. Zhang, X. Ma, J. L. Esguerra, H. Yu, O. Hjelm and J. Li, *et al.*, Towards sustainable perovskite light-emitting diodes, *Nat. Sustainability*, 2025, **8**(3), 315–324.
23 D. Yang, G. Zhang, R. Lai, Y. Cheng, Y. Lian and M. Rao, *et al.*, Germanium-lead perovskite light-emitting diodes, *Nat. Commun.*, 2021, **12**(1), 4295.
24 Y. Li, X. Guan and Y. Meng, *et al.*, Boosting $CsSnI_3$ -based near-infrared perovskite light-emitting diodes performance via solvent coordination engineering, *InfoMat*, 2024, **6**, e12537.
25 X. Guan, *et al.*, Bright and stable near-infrared lead-free perovskite light-emitting diodes, *Nat. Photonics*, 2024, **18**, 157–163.
26 X. Guan, *et al.*, Targeted elimination of tetravalent-Sn-induced defects for enhanced efficiency and stability in lead-free NIR-II perovskite LEDs, *Nat. Commun.*, 2024, **15**, 9831.
27 H. Wang, A. Treglia, M. D. Albaqami, F. Gao and A. Petrozza, Tin-Halide Perovskites for Near-Infrared Light-Emitting Diodes, *ACS Energy Lett.*, 2024, **9**, 2902–2911.
28 S. Aftab, G. Koyyada, Z. Haider, E. Akman, F. Kabir and M. Aslam, *et al.*, From lab to luminescence: Perovskite-based dimensional integrations pushing LED boundaries, *Mater. Today Phys.*, 2024, **46**, 101490.
29 B. P. Kore, M. Jamshidi and J. M. Gardner, The impact of moisture on the stability and degradation of perovskites in solar cells, *Mater. Adv.*, 2024, **5**, 2200–2217.
30 M. Chen, M. G. Ju, H. F. Garces, A. D. Carl, L. K. Ono and Z. Hawash, *et al.*, Highly stable and efficient all-inorganic lead-free perovskite solar cells with native-oxide passivation, *Nat. Commun.*, 2018, **10**(1), 16.

31 S. Rahimi, M. Eskandari and D. Fathi, New nanostructure perovskite-based light-emitting diode with superior light extraction efficiency enhancement, *Sci. Rep.*, 2024, **14**(1), 5500.
32 B. Zhao, M. Vasilopoulou, A. Fakharuddin, F. Gao, A. R. bin Mohd Yusoff and R. H. Friend, *et al.*, Light management for perovskite light-emitting diodes, *Nat. Nanotechnol.*, 2023, **18**, 981–992.
33 C. Liu, B. Li and M. Qiu, Advancements in the Improvement of Optical Outcoupling Efficiency for Perovskite LEDs, *Adv. Devices Instrum.*, 2024, **5**, 0045.
34 X. B. Shi, Y. Liu, Z. Yuan, X. K. Liu, Y. Miao and J. Wang, *et al.*, Optical Energy Losses in Organic-Inorganic Hybrid Perovskite Light-Emitting Diodes, *Adv. Opt. Mater.*, 2018, **6**(17), 1800667.
35 Q. Zhang, D. Zhang, Y. Fu, S. Poddar, L. Shu and X. Mo, *et al.*, Light Out-Coupling Management in Perovskite LEDs--What Can We Learn from the Past?, *Adv. Funct. Mater.*, 2020, **30**, 2002570.
36 M. H. Futscher and B. Ehrler, Modeling the Performance Limitations and Prospects of Perovskite/Si Tandem Solar Cells under Realistic Operating Conditions, *ACS Energy Lett.*, 2017, **2**(9), 2089–2095.
37 H. Li, Y. Zhao, J. Lu, J. Feng, J. Zhao and K. Lin, *et al.*, Phase Engineering Reinforced Energy Transfer for High-Performance Blue Perovskite Light-Emitting Diodes, *Small*, 2024, **20**(27), 2308616.
38 Z. Miao, J. Guo, D. Jiang, W. Zheng, W. Yin and Z. Luo, *et al.*, Superbly Bright Tin-Based Perovskite LEDs, *Laser Photonics Rev.*, 2024, **19**(8), 2401590.
39 N. Tabibifar, M. Eskandari, F. A. Boroumand, D. Fathi and S. Rahimi, Enhanced light extraction by optimizing near-infrared perovskite-based light emitting diode (PeLED), *Sci. Rep.*, 2024, **14**(1), 29165.
40 J. Bueno, A. Jiménez-Solano, M. Anaya and S. Carretero-Palacios, Plasmonic nanoparticles boost low-current perovskite LEDs governed by photon recycling effects, *RSC Adv.*, 2025, **15**(39), 32497–32508.
41 L. Gu, K. Wen, Q. Peng, W. Huang and J. Wang, Surface-Plasmon-Enhanced Perovskite Light-Emitting Diodes, *Small*, 2020, **16**, 2001861.
42 M. ul Ain, N. Asma, R. Ullah, Z. Fatima, A. Illahi and W. Ahmed, Engineering gold nanoworms with tunable longitudinal plasmon peak in the near infrared and their refractive index sensing properties, *RSC Adv.*, 2024, **14**(18), 12772–12780.
43 Y. Li, T. Gao, Z. He, C. Shen, S. Zhou and M. Li, *et al.*, Flexible perovskite light-emitting diodes: recent progress, applications and challenges, *npj Flexible Electron.*, 2025, **9**, 32.
44 A. Taflove, S. C. Hagness and M. Piket-May, Computational Electromagnetics: The Finite-Difference Time-Domain Method, *The Electrical Engineering Handbook*, Elsevier, 2005, pp. 629–670.
45 F. Brivio, K. T. Butler, A. Walsh and M. van Schilfgaarde, Relativistic quasiparticle self-consistent electronic structure of hybrid halide perovskite photovoltaic absorbers, *Phys. Rev. B:Condens. Matter Mater. Phys.*, 2014, **89**(15), 155204.
46 E. D. Palik, *Handbook of Optical Constants of Solids*, Academic Press, San Diego, 1985.
47 A. Alnuaimi, I. Almansouri and A. Nayfeh, Effect of mobility and band structure of hole transport layer in planar heterojunction perovskite solar cells using 2D TCAD simulation, *J. Comput. Electron.*, 2016, **15**(3), 1110–1118.
48 P. B. Johnson and R. W. Christy, Optical Constants of the Noble Metals, *Phys. Rev. B*, 1972, **6**(12), 4370–4379.
49 E. M. Purcell, H. C. Torrey and R. V. Pound, Resonance Absorption by Nuclear Magnetic Moments in a Solid, *Phys. Rev.*, 1946, **69**(1–2), 37–38.
50 Y. Cui, S. Fan, Y. Zhai, Y. Liu, J. Li and J. Hu, *et al.*, Turn-on and pinhole-free ultrathin core-shell Au@SiO2 nanoparticle-based metal-enhanced fluorescent (MEF) chemodosimeter for Hg^{2+}, *Nanoscale Adv.*, 2024, **6**, 2319–2327.
51 P. Anger, P. Bharadwaj and L. Novotny, Enhancement and Quenching of Single-Molecule Fluorescence, *Phys. Rev. Lett.*, 2006, **96**, 113002, DOI: 10.1103/PhysRevLett.96.113002.
52 S. A. Maier, *Plasmonics: Fundamentals and Applications*, Springer US, New York, NY, 2007.
53 G. Lozano, D. J. Louwers, S. R. Rodríguez, S. Murai, O. T. Jansen and M. A. Verschuuren, *et al.*, Plasmonics for solid-state lighting: enhanced excitation and directional emission of highly efficient light sources, *Light: Sci. Appl.*, 2013, **2**(5), e66.
54 J. P. Bérenger, A perfectly matched layer for the absorption of electromagnetic waves, *J. Comput. Phys.*, 1994, **114**(2), 185–200.
55 J. L. M. Priede and N. Large, Photonic band structure calculation of 3D-finite nanostructured supercrystals, *Nanoscale Adv.*, 2022, **4**(21), 4589–4596.
56 M. Gajdoš, K. Hummer, G. Kresse, J. Furthmüller and F. Bechstedt, Linear optical properties in the projector-augmented wave methodology, *Phys. Rev. B:Condens. Matter Mater. Phys.*, 2006, **73**(4), 045112.
57 E. D. Palik and G. Ghosh, *Handbook of Optical Constants of Solids*, Academic Press, 1998.
58 F. C. Wan, F. L. Tang, Z. X. Zhu, H. T. Xue, W. J. Lu and Y. D. Feng, *et al.*, First-principles investigation of the optical properties of CuIn(SxSe1-x)2, *Mater. Sci. Semicond. Process.*, 2013, **16**(6), 1422–1427.
59 S. Saha, A. Sur, L. Saha and M. K. Alam, Investigating the Optical and Thermodynamic Properties of 2D MoGe2P4: Potential Material for Photothermal Therapy, *Nano Select*, 2025, **6**(11), e70028.
60 N. Hasan, M. H. K. Anik, M. M. Hasan, S. Islam and A. Kabir, Comprehensive numerical analysis of doping controlled efficiency in lead-free CsSn1-xGexI3 perovskite solar cell, *Appl. Phys. A:Mater. Sci. Process.*, 2025, **131**(1), 34.
61 I. Chung, J. H. Song, J. Im, J. Androulakis, C. D. Malliakas and H. Li, *et al.*, CsSnI3: semiconductor or metal? High electrical conductivity and strong near-infrared photoluminescence from a single material. High hole mobility and phase-transitions, *J. Am. Chem. Soc.*, 2012, **134**(20), 8579–8587.
62 X. Zambrana-Puyalto and N. Bonod, Purcell factor of spherical Mie resonators, *Phys. Rev. B:Condens. Matter Mater. Phys.*, 2015, **91**(19), 195422.

63 D. Zhao, R. E. F. Silva, C. Climent, J. Feist, A. I. Fernández-Domínguez and F. J. García-Vidal, Impact of Vibrational Modes in the Plasmonic Purcell Effect of Organic Molecules, *ACS Photonics*, 2020, **7**(12), 3369–3375.

64 I. Vurgaftman and S. Tsoi, Purcell effect for high-Q plasmon lattice modes in the coupled dipole approximation, *J. Appl. Phys.*, 2024, **136**(5), 053102.

65 M. E. Raypah, A. A. Ahmed and A. F. Omar, Application of porous materials and structures for improving optical and thermal performance of inorganic and organic light-emitting diodes: A review, *Sens. Actuators, A*, 2022, **347**, 113966.

66 J. Katyal and V. Badoni, Localized surface plasmon resonance and field enhancement of Au, Ag, Al and Cu nanoparticles having isotropic and anisotropic nanostructure, *Mater. Today: Proc.*, 2021, **44**, 5012–5017.

67 B. Ai, Z. Fan and Z. J. Wong, Plasmonic-perovskite solar cells, light emitters, and sensors, *Microsyst. Nanoeng.*, 2022, **8**(1), 5.

68 T. Zhang, G. Lu, H. Shen, K. Shi, Y. Jiang and D. Xu, *et al.*, Photoluminescence of a single complex plasmonic nanoparticle, *Sci. Rep.*, 2014, **4**(1), 3867.

69 G. A. Wurtz, P. R. Evans, W. Hendren, R. Atkinson, W. Dickson and R. J. Pollard, *et al.*, Molecular Plasmonics with Tunable Exciton-Plasmon Coupling Strength in J-Aggregate Hybridized Au Nanorod Assemblies, *Nano Lett.*, 2007, **7**(5), 1297–1303.

70 A. Bayles, S. Carretero-Palacios, L. Calió, G. Lozano, M. E. Calvo and H. Míguez, Localized surface plasmon effects on the photophysics of perovskite thin films embedding metal nanoparticles, *J. Mater. Chem. C*, 2020, **8**(3), 916–921.

71 G. Kumar, C. C. Lin, H. C. Kuo and F. C. Chen, Enhancing photoluminescence performance of perovskite quantum dots with plasmonic nanoparticles: insights into mechanisms and light-emitting applications, *Nanoscale Adv.*, 2024, **6**(3), 782–791.

72 Z. Y. Ooi, A. Jiménez-Solano, K. Gakowski, Y. Sun, J. Ferrer Orri and K. Frohna, *et al.*, Strong angular and spectral narrowing of electroluminescence in an integrated Tamm-plasmon-driven halide perovskite LED, *Nat. Commun.*, 2024, **15**(1), 5802.

73 P. Mao, C. Liu, X. Li, M. Liu, Q. Chen and M. Han, *et al.*, Single-step-fabricated disordered metasurfaces for enhanced light extraction from LEDs, *Light: Sci. Appl.*, 2021, **10**(1), 180.

74 J. P. Martinez-Pastor, *et al.*, Strategies for Controlling Emission Anisotropy in Lead Halide Perovskite Emitters for LED Outcoupling Enhancement, *Adv. Opt. Mater.*, 2025, **37**(25), 2413622.

75 W. Bai, T. Xuan, H. Zhao, H. Dong, X. Cheng and L. Wang, *et al.*, Perovskite Light-Emitting Diodes with an External Quantum Efficiency Exceeding 30%, *Adv. Mater.*, 2023, **35**(39), 2302283, DOI: 10.1002/adma.202302283.

76 L. Lin, Q. Li and T. Zhang, *et al.*, Photonic cavity effects for enhanced efficiency in layered perovskite-based light-emitting diodes, *Nanomaterials*, 2021, **11**, 2947.

77 R. He, M. Meunier, Z. Dong, H. Cai, W. Gao and J. Zuniga-Perez, *et al.*, Interplay of Purcell effect and extraction efficiency in $CsPbBr_3$ quantum dots coupled to Mie resonators, *Nanoscale*, 2023, **15**, 1652–1660.